

# TOWARDS AN AUTOMATIC ANALYSIS OF CHO-K1 SUSPENSION GROWTH IN MICROFLUIDIC SINGLE-CELL CULTIVATION

PREPRINT, COMPILED NOVEMBER 13, 2021

DOMINIK STALLMANN

JAN P. GÖPFERT

JULIAN SCHMITZ

ALEXANDER GRÜNBERGER

BARBARA HAMMER

Bielefeld University, Germany

## ABSTRACT

**Motivation:** Innovative microfluidic systems carry the promise to greatly facilitate spatio-temporal analysis of single cells under well-defined environmental conditions, allowing novel insights into population heterogeneity and opening new opportunities for fundamental and applied biotechnology. Microfluidics experiments, however, are accompanied by vast amounts of data, such as time series of microscopic images, for which manual evaluation is infeasible due to the sheer number of samples. While classical image processing technologies do not lead to satisfactory results in this domain, modern deep learning technologies such as convolutional networks can be sufficiently versatile for diverse tasks, including automatic cell tracking and counting as well as the extraction of critical parameters, such as growth rate. However, for successful training, current supervised deep learning requires label information, such as the number or positions of cells for each image in a series; obtaining these annotations is very costly in this setting.

**Results:** We propose a novel Machine Learning architecture together with a specialized training procedure, which allows us to infuse a deep neural network with human-powered abstraction on the level of data, leading to a high-performing regression model that requires only a very small amount of labeled data. Specifically, we train a generative model simultaneously on natural and synthetic data, so that it learns a shared representation, from which a target variable, such as the cell count, can be reliably estimated.

**Availability:** The project is cross-platform, open-source and free (MIT licensed) software. We make the source code available at [https://github.com/dstallmann/cell\\_cultivation\\_analysis](https://github.com/dstallmann/cell_cultivation_analysis); the data set is available at <https://pub.uni-bielefeld.de/record/2945513>

**Contact:** [dstallmann@techfak.uni-bielefeld.de](mailto:dstallmann@techfak.uni-bielefeld.de)

## 1 INTRODUCTION

New and improved single-cell analysis technologies employing live cell imaging allow researchers to acquire cellular information with ever-increasing levels of detail [9]. Especially for the study of cellular heterogeneity in clonal populations, which has long been ignored, single-cell applications are mandatory. Here, Microfluidic Single-cell Cultivation (MSCC) in particular is a promising tool to analyze single-cell behavior [23]. Due to its microfluidic setup, MSCC allows for maintaining clearly defined cultivation environments or even dynamic changes of cultivation conditions [16]. Furthermore, MSCC encompasses live cell imaging and thereby allows systematic single-cell studies with high spatial and temporal resolution of cellular behavior.

Despite its beneficial features for single-cell analysis, MSCC comes with a major bottleneck: enormous amounts of detailed data are generated that need processing. So far, image analysis has mostly been performed manually or semi-manually. Therefore, MSCC requires adaptations with regards to the processing of the data produced. This either means the training of human experts and resulting extensive labor, or the development of new algorithms, where current approaches typically require either careful tuning or manually labeled data for training. In the long run, this is not feasible, and different, more affordable computer vision solutions are required [26].

In recent years, deep neural networks, in particular convolutional neural networks, which naturally mirror spatial priors, have been established as the standard technology for automated image

processing and computer vision [13], and a considerable number of applications can be found in the biomedical domain [19]. While trained deep networks models such as YOLO, VGG, or ResNet are readily available for natural scenes, these models do not easily transfer to other domains or imaging technologies, due to the different statistical properties observed in these fields. There exist a number of approaches that tackle the challenge to track cells in images [18]:

Fundamental progress has been made by proposing a benchmark suite based on different imaging technologies and comparing the strengths and limitations of diverse methods for cell tracking [28]. Still, one conclusion is the observation that automatic tracking remains prone to errors, and the tuning of model parameters for novel domains can be very cumbersome. The approach [3] enables an interactive bioimage analysis framework for intuitive user interaction. The work [12] focuses on the challenge of gathering labeled data by providing a crowd based annotation tool, which allows a distribution of the work of manual labeling, based on which deep learning becomes possible. Interestingly, the work [4] displays the possibility to transfer results in between different imaging technologies to some extent. The approach [7] provides one of the few toolboxes for cell tracking, which allows transfer learning based on given models and novel data, whereby data set enrichment technologies limit the number of required samples. Yet, the data used consists of adherent cells rather than suspension cells.

In contrast to already reported studies [6] and [16], where adherent growing cell lines were the focus of investigation, in

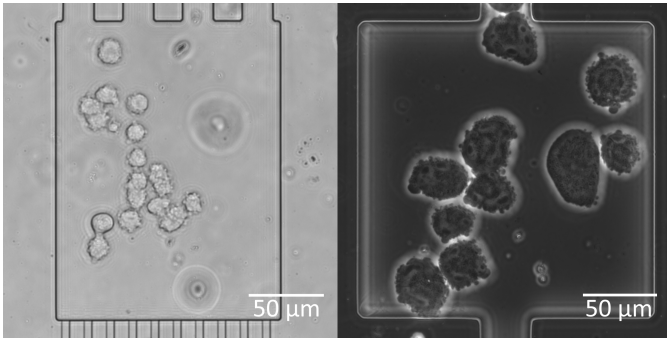


Figure 1: Samples from the data sets. Bright-field microscopy image on the left, phase-contrast microscopy image on the right. Faint and very small circles are smudges on the chip. The architecture has to differentiate between cells, smudges and background. Translational and rotational camera drift has been removed by semi-automatic image processing beforehand. The crop intentionally allows for data augmentation techniques to crop the images further.

this study we will concentrate on suspension cells, for which analysis tools of adherent cells are insufficient: suspension cells have a circular basic shape but ever-changing contour due to vesicle secretion and the addition of cell movement and floating within the chamber complicates tracking and analysis processes. Automatic analysis of these cells growing in suspension comes with different and challenging obstacles, which will be described in Section 2.

Due to this fact, we cannot transfer existing models, such as the ones mentioned above, to the given setting. We are interested in the question how to automatically provide sufficiently accurate cell counting, based on which the process dynamics can be characterized. We will use deep convolutional networks for this task. Unlike existing technologies, which are typically fully supervised, we put a particular focus on the challenge to mitigate the cumbersome task of manual labeling. We propose a new deep twin auto-encoder architecture, which enriches the training data by artificial geometric data, for which ground truth labeled data can easily be generated. The proposed twin architecture greatly reduces the cost of synthetic, auxiliary training data, because that data does not need to appear realistic in all regards, such as morphological details and fidelity.

Training is based on a novel cost function that enriches the final task of cell counting by the challenge of correct representations. Optimization of this architecture is partially based on auto-ML technologies [10].

## 2 MATERIAL AND METHODS

### 2.1 MSCC and live cell imaging data

Image data applied in this study was obtained by single-cell cultivation of mammalian suspension cells (MaSC) [24]. CHO-K1 cells were cultivated in polydimethylsiloxane (PDMS)-glass-chips and constantly provided with nutrients by perfusion of the microfluidic device. Live cell imaging was accomplished with an automated inverted microscope (Nikon Eclipse Ti2,

Nikon Instruments, Germany), every 20 minutes time lapse images of relevant positions on-chip were taken (NIS Elements AR 5.20.01 Software, Nikon Instruments, Germany). In the following, the data used in this work is split into two parts according to the two microscopy technologies that were used for the analysis of the cells (see Figure 1). Data set A consists of bright-field microscopy images and contains 12 scenarios accumulating to 5202 images, of which 1.4 % are labeled. Data set B consists of phase-contrast microscopy images and contains 37 scenarios, accumulates to 11 189 images, of which 5.9 % are labeled. The labels were created in a regular interval over the data sets. Images with more than 30 cells were removed beforehand, since at this count, the outcome of the cultivation experiment is determined.

Since the focus of this work lies on the bigger data set B, Figure 2 shows the relation between the amount of cells that are present in images of the test data related to the number of images that contain the according number of cells for that data set. The present labels are mostly used for tests and verification, rather than training, since we aim for a technology that requires few manual labels. For data set B, only 1.87 % of the training data is labeled, while 50 % of the test and verification data is labeled, to ensure a meaningful generalization for the results. The images have been cropped and rotated to center the cultivation chamber. Data augmentations which are not part of this preprocessing were applied as described in Section 2.3.3.

Among the more challenging aspects in the cultivation of suspension cells, in comparison to adherent cells, are the large number of visual characteristics, which prevent traditional cell counting techniques and tracking approaches [20]. As can be seen in Figure 1, there are a multitude of visual effects that complicate the automated counting process. Often, certain of these characteristics are being tackled, such as varying contrast and light conditions [5], or cells sticking together and overlapping each other [30], but additional ongoing cell divisions and changes in shape due to secretion of vesicles, which makes their silhouettes highly irregular, impede the process and diminish the applicability of state-of-the-art solutions. Furthermore, appearing and vanishing of cells through the passages of the chamber, a potential overpopulation of the culture and differing focus plains based on the cells' dimensions and inner organelles, make intracellular compartment non-uniform, further increasing the challenge to automate counting.

### 2.2 Approach

Our aim is the inference of a technology which, given data with only few manual annotations, yields a reliable deep network for cell counting for suspension cell microscopic images. The challenge to learn from mostly unlabeled data, which are enriched by few manual labels, is usually referred to as semi-supervised learning. We will propose a novel technology to mitigate this complexity, by introducing synthetic data with known ground truth and a twin architecture, which can abstract from the fact that these enrichments are synthetic. We will now describe how we generate the data set enrichment, first, and introduce the specific neural architecture thereafter.

Since semi-supervised learning is a balancing act between reducing the share of labels required for acceptable results and

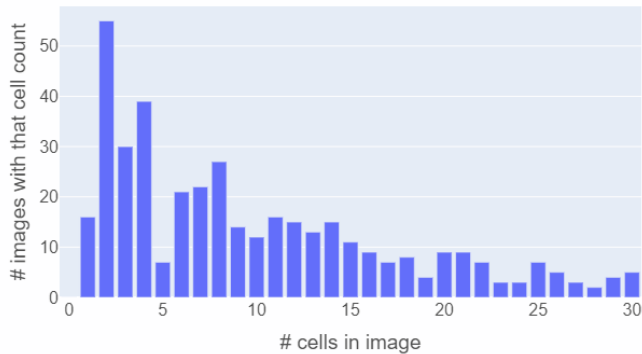


Figure 2: Visualization of the natural test data for data set B, displaying the distribution of images that contain a given number of cells. Images with more than 30 cells have been omitted due to loss in relevance for the cultivation experiments.

increasing the share of labels to achieve desirable results [21], an additional dimension can be opened to tackle the problem from another side: we propose to enrich the training set with synthetic data, for which the ground truth is known because it is based on explicit geometric modeling, thereby simplifying the geometric heterogeneity of real suspension cells drastically. Synthetic data has already successfully been used to improve the performance of artificial neural networks, e. g., for text processing [14]. Unlike data set enrichment, which directly enriches given data, synthetic data enables us to create a large variety of samples, which is not limited by the real data.

One might try to synthetically generate images that are indistinguishable from real ones. This would entail a considerable amount of engineering [8]. Instead, we rely only on basic geometric shapes to represent cells, neglecting concrete texture and intricate morphology. In the following, we show that this is adequate for successful training using our neural twin architecture (Section 2.2) and it actually allows us to introduce our abstraction into the data: cells (in these kinds of images) can be represented by ellipses, especially when the objective is to count them.

Examples of the synthetic images can be seen in Figure 3. The cell distribution in these images is close, but not identical, to the one of the natural data sets. These images are generated algorithmically with seed consistency, so they can be reproduced. We constructed as many synthetic images as there exist real ones for the sake of balance. The background is created by taking the mean of all natural training images with few cells (to ensure high visibility of the background). The synthetic images are generated in the 128 by 128 pixels working resolution of the architecture described in Section 2.2 and their size is about 8 MB per 1000 images. The generator is fully adjustable, creating images with a given distribution of cell counts, controls overlapping of cells, varies the brightness of the cell’s inner organelles their membrane silhouette and the background, etc., such as in the natural data. Smudges, as in Figure 1, have not been inserted, since they are an interference factor and are assumed to only hinder the training process. The cells have been given a circular shape to roughly match the shape of the natural cells. Some stretching or deforming to ellipses, noise, brightness

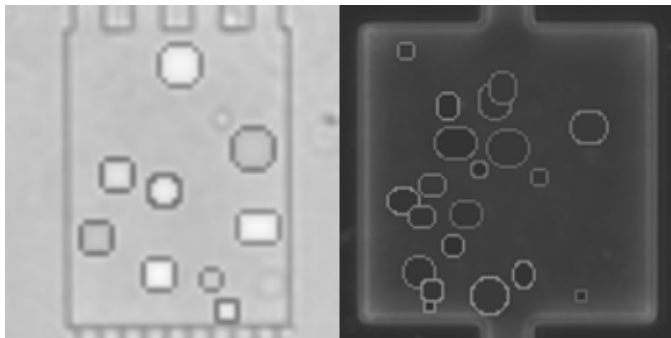


Figure 3: Samples of synthetic data from the proxy data set. Bright-field microscopy image on the left, phase-contrast microscopy image on the right. The images do not show scale bars, because they are dimensionless. A theoretical size could be calculated in relation to the chamber size, but it is of no importance for the work.

fluctuation and Gaussian filters of varying strengths have been added to increase the variety of cells in the data. This geometric form can easily be adjusted if natural cells in other data sets have different shape characteristics.

### 2.3 Network Architecture & Training

#### 2.3.1 Architecture

We propose a novel architecture that bypasses the problem of difference in appearance of synthetic and natural images, by separating the input of data for training depending on their origin, but requiring the architecture to create a tightly coupled shared inner representation to prevent high training losses. We do so by creating two identical variational autoencoders (VAE) for the two data sets, sharing the weights of their last layer of the encoder, the first layer of the decoder and the bottleneck in-between (see Figure 4). VAEs are the state-of-the-art solution for generalized few-shot learning [25] and weight-sharing has been used to reduce neural network sizes and to improve test performance before [27].

One of the VAEs uses synthetic data (*VAE-syn*), while the other one handles natural data only (*VAE-nat*). The different visual characteristics of synthetic and natural data are accounted for in the non-shared layers, while the shared layers rely on and enforce a common representation of relevant image characteristics. Besides auto-encoding, the architecture acts in a supervised way for data with known labels, by adding a two-layer-deep fully connected neural network regression model for the actual cell counting, based on the shared representation of the VAEs. Cell detection by regression has been shown to work well for other (less demanding) tasks [31, 30].

Our architecture addresses two objectives simultaneously:

- Encoding as well as decoding natural and synthetic input images using a shared representation.
- Predicting the present cell count for both types of images.

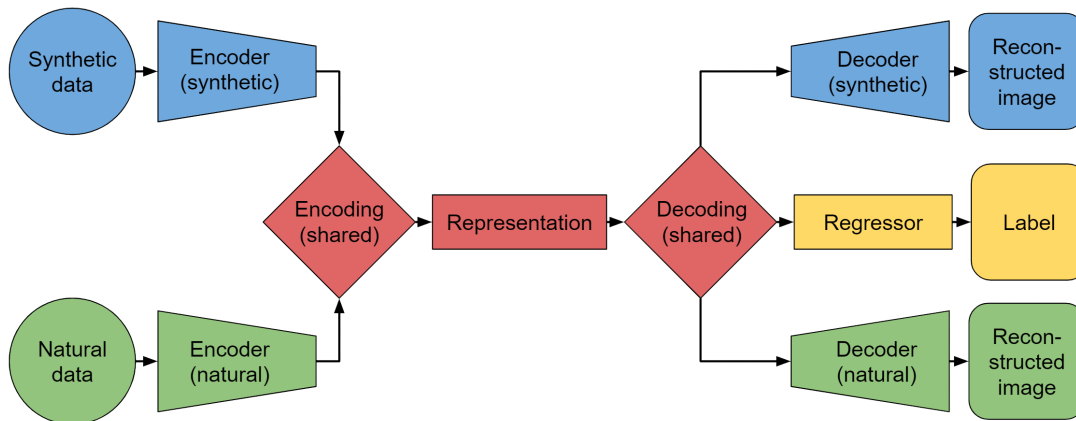


Figure 4: Visualization of the weight shared VAE twin. The blue elements handle synthetic data, while the green elements handle natural data. The red elements are shared between the two VAEs and contain the inner representation of the cell imagery, while the yellow elements result in an estimation for the cell count.

### 2.3.2 Loss

Given an input image  $x$  of pixels, a label (i. e., cell count)  $l$  between 1 and 30 and a type  $t \in \{n, s\}$ , representing the fact whether the image is natural or synthetic, we obtain a reconstruction loss  $\text{Rec}(x)$  of the VAE, a regression loss  $\text{Reg}(x, l)$  of the task at hand such as cell counting, and a distributional regularization loss  $\mathcal{D}_{\text{KL}}$ , which aims for a homogeneous representation of synthetic and real data in the embedding space of the VAE. We combine these losses to form our twin loss  $\text{Twin}_{\text{loss}}(x, l, t)$  with weighting factors  $C_{\text{Rec}}^t$ ,  $C_{\text{Reg}}^{t,l}$ , and  $C_{\mathcal{D}_{\text{KL}}}^t$ , respectively, which allows us to balance the impacts between natural and synthetic images and to gracefully handle input images without known cell counts by setting  $C_{\text{Reg}}^{t,l}$  to zero:

$$\text{Twin}_{\text{loss}}(x, l, t) = C_{\text{Rec}}^t \cdot \text{Rec}(x) + C_{\text{Reg}}^{t,l} \cdot \text{Reg}(x, l) + C_{\mathcal{D}_{\text{KL}}}^t \cdot \mathcal{D}_{\text{KL}}(x) \quad (1)$$

During our experiments, the mean-squared error (MSE)  $\|x - d(x)\|^2$ , where  $d(x)$  is the reconstruction of the input image  $x$  and  $\|l - r(x)\|^2$ , where  $r(x)$  is the estimated cell count, yielded the best results respectively, when used as  $\text{Rec}(x)$  and  $\text{Reg}(x, l)$  for training on phase-contrast data, and as  $\text{Reg}(x, l)$  for bright-field data. However, for bright-field data the binary cross entropy (BCE)  $-l \cdot \log(r(x)) + (1 - l) \cdot \log(1 - r(x))$  turned out to be the superior choice for  $\text{Rec}(x)$  and was often resulting in just slightly worse results than the MSE for phase-contrast data. The  $\mathcal{D}_{\text{KL}}$  is applied in the form of the Kullback-Leibler divergence (KLD) of the standard VAE ([15]) and is needed to generate latent vectors that are sufficiently close to a normal distribution. The weighting factors  $C_{\text{Rec}}^t$ ,  $C_{\text{Reg}}^{t,l}$ , and  $C_{\mathcal{D}_{\text{KL}}}^t$  have to be chosen carefully for training to succeed, punishing incorrect cell count predictions especially on natural cells, while relaxing the importance of visual reconstruction. We provide details in the following section.

### 2.3.3 Neural Network

The non-shared part of the encoder consists of four two-dimensional convolutional layers with kernel size 5 and stride 2,

and are initialized with an orthogonal basis [22]. Between the layers are leaky rectified linear units (ReLU) with a leakiness of 0.2 as well as dropout of 0.1. The amount of channels used for the convolutions are 32, 64, 128 and 256, in this order, for the encoders. The shared part of the encoder has an additional two-dimensional convolutional layer with the same properties and 512 channels. The layer is followed by the bottleneck, which consists of three layers of fully connected neurons of sizes 512, 256 and 512 again, each with a dropout of 0.1. The shared part of the decoder has 256 channels, uses a two-dimensional transposed convolutional operator layer with the same kernel size and stride as above, and is followed by a batch normalization over a four-dimensional input and another leaky ReLU with a leakiness of 0.2. The non-shared part of the decoder consists of five layers of kernel sizes 5, 5, 5, 2, 6, a continuous stride of 2 except for the fourth layer with a stride of 1, the same leaky ReLUs and a sigmoidal activation function at the end. The output of the shared part of the decoder is also fed to a two-layer fully connected branch of neurons for the regressor of sizes 256 and 128. The regressor uses linear layers and a dropout of 0.1.

The architecture is using the Adam optimizer for phase-contrast microscopy data, and the rectified Adam (RAdam) [17] optimizer for bright-field data. The combination of the decoder loss factor  $C_{\text{Rec}} = 100$ , the regressor loss factor  $C_{\text{Reg}} = 3$  and the KLD factor  $C_{\mathcal{D}_{\text{KL}}} = 2$  yield the best results for phase-contrast data. For the BCE, the decoder loss factor is not constant, but decays over time with a rate of  $3 \times 10^{-5}$  per epoch, since the BCE will not decrease significantly within the training process, but needs to decrease over time to amplify the importance of low regression losses  $\text{Reg}(x, l)$ .

While it seems counter-intuitive that  $C_{\text{Rec}}$  is bigger than  $C_{\text{Reg}}$  and  $C_{\mathcal{D}_{\text{KL}}}$ , it is caused by the MSE for pixel data getting very small on normalized images and it's actually being a desirable factor for the KLD to stay relatively small, since it is required to enhance the quality of the distributions, but should not impact the training of cell predictions too much by unfortunate sampling from the latent vector. Additionally a soft weight decay of  $1 \times 10^{-5}$  per epoch, a fixed learning rate of  $1.3 \times 10^{-4}$  and a delayed start for the regressor of 100 epochs were used to achieve the results presented in Section 3. A batch size of 128 for the phase-contrast

images and 64 for the bright-field images worked best and the training runs for up to 50.000 epochs, unless early stopping conditions abort it.

To minimize the number of hyperparameters that had to be optimized by hand, a Bayesian optimization in form of a Gaussian Process regressor [29] has been used to find good values for the learning rate, the number of channels of the bottleneck and the convolutional layers around it, as well as all three loss weight factors.

### 2.3.4 Data Augmentation

To maximize the use of the limited amounts of natural data, multiple data augmentation techniques were combined and applied to the data. Random horizontal and vertical flips are combined with a random resized crop of scale 0.9, meaning the images get randomly cropped to 115 by 115 pixels and then scaled back to 128 by 128 pixels. While the crop does add difficulty to the cell detection process by allowing cells to be at positions where, without the crop, only the chamber border and outside of the chamber would be, it proved necessary to establish the possibility of cells appearing anywhere on the image, assuring equalized detection success, barely impacted by the cell position within the image. Then, a 90 degree rotation is applied at random and a zero-centered noise map is generated and added to the image with a small amplitude factor.

## 3 RESULTS

### 3.1 Cell counting & Reconstruction

Table 1 shows that the proxy data can be used to significantly improve the test performance in both sets of data, compared to state-of-the-art semi-supervised deep learning without synthetic data. Therefore, the technique proves reliability for different types of cells and microscopy technologies. 57.8 % of the natural test images are counted correctly for the main data set. To clarify this, we added the DEV-nat and MAE-nat values. DEV-nat shows an average absolute deviation between prediction and true cell count of 5.66 %. Considering that images contain 1 to 30 cells, the error is often small enough to be removed fully, when the prediction is rounded to the nearest full number. MAE-nat (mean average error of natural data) confirms a 0.59 absolute average miscount. For each data set, meta parameters were found that optimize MAE-nat and DEV-nat more, but have a decreased correct counting rate, suggesting a tendency of overfitting towards a sub range of cell counts.

The average deviation of the predicted cell counts compared to the ground truth for the natural test data set is visualized in Figure 5. It can be seen that the average deviation is mostly stable for all cell counts and only starts to increase slightly for high cell counts, presumably caused by more densely filled chambers and therefore increased cell overlaps, slim borders etc.

Further, Figure 6 shows an example of an optimal reconstruction, i. e., the cell count estimation is correct and visually matches the reconstructed image. Note that unimportant visual details of the cells are not reconstructed and an abstraction of the cell boundaries to simpler geometries is applied. Hence, the network has learned to remove most unnecessary information from the

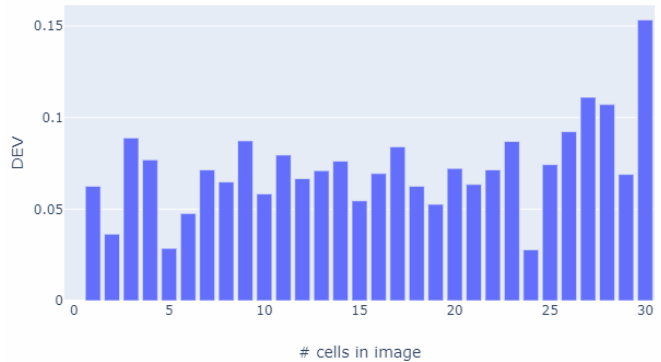


Figure 5: The relative deviation of cell counts in natural images of the test data set. The average error is about 7 % to 8 %, with a light tendency towards better counts for images with fewer cells.

internal representation, which allows the architecture to work well on unseen cells that differ in these categories. The figure also shows that the topmost smudge has been reconstructed, but its impact was not big enough to mislead the architecture to a wrong prediction.

Figure 7 shows an example of a suboptimal reconstruction. In this case, two cells that clumped together were interpreted as one cell (as can be seen in the reconstruction on the right). The network did not detect the slim border between the cells and therefore reconstructed it as a single, bigger cell.

### 3.2 Representation

To verify the similarity of representations for both types of data, we propagate one type of data to the decoder of the other type and see that the visual style of the cells has changed, while the cell count and transformation (i. e., position and size) stay similar (see Figure 8 and Figure 9). While this does connote a certain commonality between representations, it is only vague and can be confirmed by a UMAP (see Figure 10). The figure additionally shows that images with similar or identical cell counts are projected near to each other, implying relative independence of the type of data that is handed to the network and focus on the actual content, i. e., the cell count.

Table 1: Experimental results: Natural data only (NDO) acts as baseline for the state of the art few-shot learning result, synthetic data set support (SDS) shows a significant boost in performance by using the proxy data set. The number suffix represents different runs on unique hyperparameter-sets.

| Variant             | MAE-syn     | DEV-syn      | Cor-syn      | MAE-nat     | DEV-nat      | Cor-nat      |
|---------------------|-------------|--------------|--------------|-------------|--------------|--------------|
| Phase-contrast data |             |              |              |             |              |              |
| NDO                 | N/A         | N/A          | N/A          | 1.07        | 20.1%        | 39.8%        |
| SDS1                | <b>0.09</b> | <b>0.68%</b> | <b>68.2%</b> | 0.60        | 5.92%        | <b>57.8%</b> |
| SDS2                | 0.14        | 0.73%        | 62.1%        | <b>0.59</b> | <b>5.66%</b> | 57.0%        |
| Bright-field data   |             |              |              |             |              |              |
| NDO                 | N/A         | N/A          | N/A          | 0.91        | 13.3%        | 23.4%        |
| SDS1                | <b>0.48</b> | <b>4.27%</b> | <b>60.1%</b> | 0.68        | 7.60%        | <b>53.2%</b> |
| SDS2                | 0.52        | 4.63%        | 58.2%        | <b>0.63</b> | <b>7.31%</b> | 51.9%        |

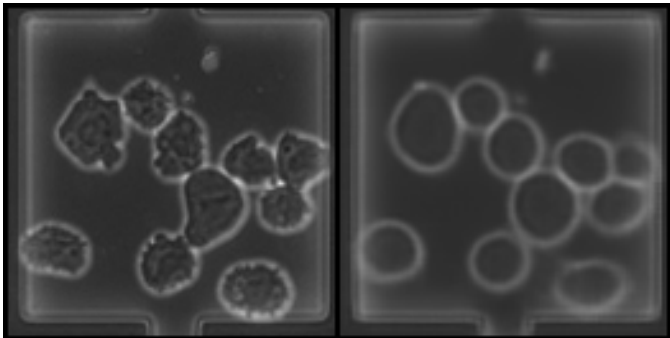


Figure 6: Examples of an optimal reconstruction of a natural images. Left side is original, right side reconstruction. The cell count matches the label and a connection between the visual reconstruction and the cell count delineates.

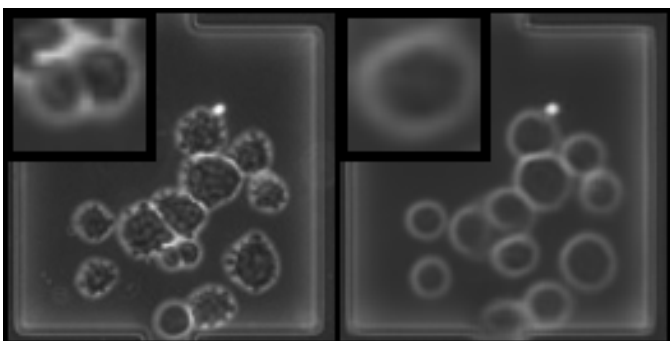


Figure 7: Examples of a suboptimal reconstruction of a natural images. Left side is original, right side reconstruction. The cell count differs from the label by one, suggesting that a merge of two small cells not only happened visually, but also semantically.

#### 4 DISCUSSION

With this architecture we do not only provide a workflow for offline image recognition of suspension cells. This lays the foundation for automated cell counting of microfluidic cell cultivations with single-cell resolution obtained by life-cell imaging and can be extended to continuously estimate cell counts in real-

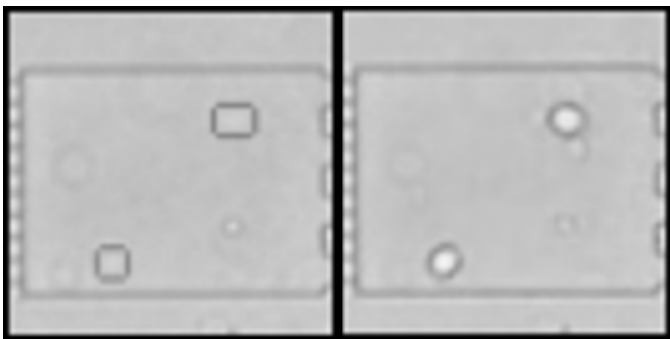


Figure 8: Sample of a conversion from synthetic data (left) to natural data (right). One can see, that the visual style of the natural cells has been applied, while boundary conditions like positions, cell count and cell sizes are widely unchanged.

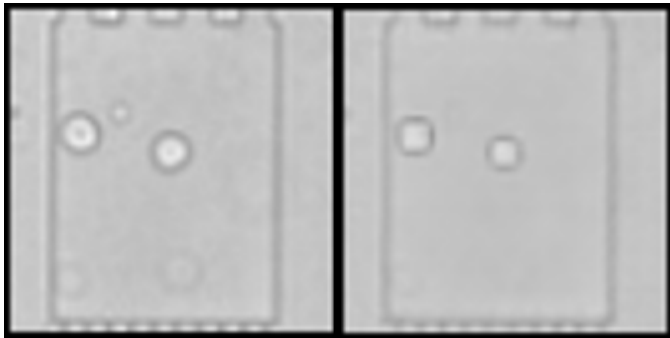


Figure 9: Sample of the opposing conversion, i. e., from natural data (left) to synthetic data (right). In this case, smudges, which are not present in the synthetic data set, are removed from the background. All other visual effects, described in Figure 8 also occur here.

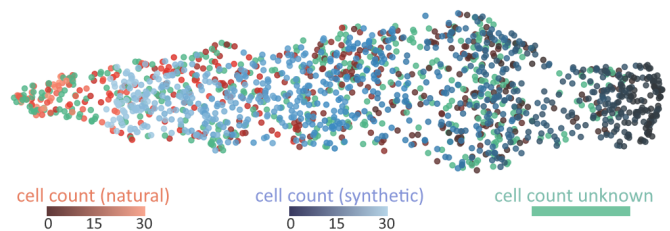


Figure 10: Embedding of learned representations, computed via UMAP. Visible are 392 natural samples (red circles) and 794 synthetic samples (blue circles) with the respective cell count indicated by lightness. Darker colors indicate lower cell counts. Additionally, we include 394 natural samples without known cell counts (green circles). Note that the circles get darker from left to right, so this direction (determined to be important by UMAP) directly corresponds to the cell count. At the same time, natural and synthetic samples are not separated, which would contradict a truly shared representation between the two types of images.

time for experimentation monitoring and prediction of additional relevant information (e. g., survivability of a culture, growth rate or doubling time etc.). Since the technique works independent of the real world size of the cells, it is possible to generate proxy data for completely different kinds of cells (e. g., bacterial) with slight adjustments to the synthetic data generator. To reduce the amount of hand crafting meta-parameters further, the Gaussian process regressor can be extended, to allow provision of an easy to use tool, to be operated by biologists as an end-to-end solution for cell counting in live cell imaging procedures.

The novel twin-VAE presented in this paper can be expanded on, e. g., by implementing an interactive manual counting to improve performance similar to [1], which could decrease the training time or even improve the overall results. As the presumably biggest challenge to overcome, overlapping of cells can be tackled with the methods presented in [2]. Another option is to extend on data augmentation instead of explicit regularization [11].

#### 4.1 Limitations

For cells that appear very small in the images, the architecture currently can not deliver low error estimations, especially if the cells are only few pixels big in the downscaled version of the images. For bright-field data, cells sticking to the walls are a bigger hindrance to precise estimations, since, unlike for phase-contrast cells, there often is little to no visual hint for the boundary between the chamber border and the cell membrane. These problems can presumably be overcome with relative ease by more image preprocessing, like gray-value equalization.

Due to the high number of hyperparameter choices combined with the on average three day long training cycle per parameter-set, the Gaussian Process regression is currently infeasible to be used to optimize all hyperparameters. However, it has proven useful to parallelize multiple runs and create a new range of hyperparameter options based on the best results of the previous iteration. The technique shows promise to reduce the number of training cycle iterations needed but currently requires alternating between automation and handcrafting.

#### REFERENCES

- [1] Carlos Arteta, Victor Lempitsky, J. Alison Noble, and Andrew Zisserman. “Interactive Object Counting”. In: *Computer Vision – ECCV 2014*. Ed. by David Fleet, Tomas Pajdla, Bernt Schiele, and Tinne Tuytelaars. Vol. 8691. Series Title: Lecture Notes in Computer Science. Cham: Springer International Publishing, 2014, pp. 504–518. ISBN: 978-3-319-10577-2 978-3-319-10578-9. DOI: [10.1007/978-3-319-10578-9\\_33](https://doi.org/10.1007/978-3-319-10578-9_33). URL: [http://link.springer.com/10.1007/978-3-319-10578-9\\_33](http://link.springer.com/10.1007/978-3-319-10578-9_33).
- [2] Carlos Arteta, Victor Lempitsky, J. Alison Noble, and Andrew Zisserman. “Detecting overlapping instances in microscopy images using extremal region trees”. In: *Medical Image Analysis* 27 (2016), pp. 3–16. ISSN: 1361-8423. DOI: [10.1016/j.media.2015.03.002](https://doi.org/10.1016/j.media.2015.03.002).
- [3] Stuart Berg et al. “ilastik: interactive machine learning for (bio)image analysis”. In: *Nature Methods* 16.12 (2019), pp. 1226–1232. DOI: [10.1038/s41592-019-0582-9](https://doi.org/10.1038/s41592-019-0582-9).
- [4] Roger Brent and Laura Boucheron. “Deep learning to predict microscope images”. In: *Nature Methods* 15.11 (2018), pp. 868–870. DOI: [10.1038/s41592-018-0194-9](https://doi.org/10.1038/s41592-018-0194-9).
- [5] Steven W. Chen, Shreyas S. Shivakumar, Sandeep Dcunha, Jnaneshwar Das, Edidiong Okon, Chao Qu, Camillo J. Taylor, and Vijay Kumar. “Counting Apples and Oranges With Deep Learning: A Data-Driven Approach”. In: *IEEE Robotics and Automation Letters* 2.2 (Apr. 2017), pp. 781–788. ISSN: 2377-3774. DOI: [10.1109/LRA.2017.2651944](https://doi.org/10.1109/LRA.2017.2651944).
- [6] Dino Di Carlo, Liz Y Wu, and Luke P Lee. “Dynamic single cell culture array”. In: *Lab on a Chip* 6.11 (2006), pp. 1445–1449. DOI: [10.1039/b605937f](https://doi.org/10.1039/b605937f).
- [7] Thorsten Falk et al. “U-Net: deep learning for cell counting, detection, and morphometry”. In: *Nature Methods* 16.1 (2019), pp. 67–70. DOI: [10.1038/s41592-018-0261-2](https://doi.org/10.1038/s41592-018-0261-2).
- [8] Jan Philip Göpfert, Christina Göpfert, Mario Botsch, and Barbara Hammer. “Effects of variability in synthetic training data on convolutional neural networks for 3D head reconstruction”. In: *2017 IEEE Symposium Series on Computational Intelligence (SSCI)*. IEEE, 2017, pp. 1–7. DOI: [10.1109/SSCI.2017.8285305](https://doi.org/10.1109/SSCI.2017.8285305).
- [9] Alexander Grünberger, Wolfgang Wiechert, and Dietrich Kohlheyer. “Single-cell microfluidics: opportunity for bioprocess development”. In: *Current Opinion in Biotechnology* 29 (2014). Cell and Pathway Engineering, pp. 15–23. ISSN: 0958-1669. DOI: [10.1016/j.copbio.2014.02.008](https://doi.org/10.1016/j.copbio.2014.02.008).
- [10] Xin He, Kaiyong Zhao, and Xiaowen Chu. *AutoML: A Survey of the State-of-the-Art*. 2020. arXiv: [1908.00709](https://arxiv.org/abs/1908.00709).
- [11] Alex Hernández-García and Peter König. *Data augmentation instead of explicit regularization*. 2018. arXiv: [1806.03852](https://arxiv.org/abs/1806.03852).
- [12] Alex J. Hughes, Joseph D. Mornin, Sujoy K. Biswas, Lauren E. Beck, David P. Bauer, Arjun Raj, Simone Bianco, and Zev J. Gartner. “Quanti.us: a tool for rapid, flexible, crowd-based annotation of images”. In: *Nature Methods* 15.8 (2018), pp. 587–590. DOI: [10.1038/s41592-018-0069-0](https://doi.org/10.1038/s41592-018-0069-0).
- [13] Anastasia Ioannidou, Elisavet Chatzilari, Spiros Nikolopoulos, and Ioannis Kompatsiaris. “Deep Learning Advances in Computer Vision with 3D Data: A Survey”. In: *ACM Comput. Surv.* 50.2 (Apr. 2017). ISSN: 0360-0300. DOI: [10.1145/3042064](https://doi.org/10.1145/3042064).
- [14] Max Jaderberg, Karen Simonyan, Andrea Vedaldi, and Andrew Zisserman. *Synthetic data and artificial neural networks for natural scene text recognition*. Workshop on Deep Learning, Advances in Neural Information Processing Systems (NIPS); Palais des Congrès de Montréal, Montréal Canada. 2014. arXiv: [1406.2227](https://arxiv.org/abs/1406.2227).
- [15] Diederik P Kingma and Max Welling. *Auto-Encoding Variational Bayes*. 2013. arXiv: [1312.6114](https://arxiv.org/abs/1312.6114).
- [16] Martin Kolnik, Lev S Tsimring, and Jeff Hasty. “Vacuum-assisted cell loading enables shear-free mammalian microfluidic culture”. In: *Lab on a chip* 12.22 (2012), pp. 4732–4737. DOI: [10.1039/C2LC40569E](https://doi.org/10.1039/C2LC40569E).
- [17] Liyuan Liu, Haoming Jiang, Pengcheng He, Weizhu Chen, Xiaodong Liu, Jianfeng Gao, and Jiawei Han. *On the Variance of the Adaptive Learning Rate and Beyond*. 2020. arXiv: [1908.03265](https://arxiv.org/abs/1908.03265).
- [18] Erick Moen, Dylan Bannon, Takamasa Kudo, William Graf, Markus Covert, and David Van Valen. “Deep learning for cellular image analysis”. In: *Nature Methods* 16.12 (2019), pp. 1233–1246. DOI: [10.1038/s41592-019-0403-1](https://doi.org/10.1038/s41592-019-0403-1).
- [19] Muhammad Imran Razzak, Saeeda Naz, and Ahmad Zaib. “Deep Learning for Medical Image Processing: Overview, Challenges and the Future”. In: *Classification in BioApps: Automation of Decision Making*. Cham: Springer International Publishing, 2018, pp. 323–350. ISBN: 978-3-319-65981-7. DOI: [10.1007/978-3-319-65981-7\\_12](https://doi.org/10.1007/978-3-319-65981-7_12).
- [20] Jason Riordon, Dušan Sovilj, Scott Sanner, David Sinton, and Edmond W. K. Young. “Deep Learning with Microfluidics for Biotechnology”. In: *Trends in Biotechnology* 37.3 (2019), pp. 310–324. ISSN: 0167-7799. DOI: [10.1016/j.tibtech.2018.08.005](https://doi.org/10.1016/j.tibtech.2018.08.005).
- [21] Deepak Babu Sam, Neeraj N. Sajjan, Himanshu Maurya, and R. Venkatesh Babu. “Almost Unsupervised Learning for Dense Crowd Counting”. In: *Proceedings of the AAAI Conference on Artificial Intelligence* 33.1 (July 17, 2019), pp. 8868–8875. ISSN: 2374-3468. DOI: [10.1609/aaai.v33i01.33018868](https://doi.org/10.1609/aaai.v33i01.33018868).
- [22] Andrew M Saxe, James L McClelland, and Surya Ganguli. “Exact solutions to the nonlinear dynamics of learning in deep linear neural networks”. In: *International Conference on Learning Representations*. 2013. arXiv: [1312.6120](https://arxiv.org/abs/1312.6120).

- [23] Julian Schmitz, Thomas Noll, and Alexander Grünberger. “Heterogeneity Studies of Mammalian Cells for Bioproduction: From Tools to Application”. In: *Trends in Biotechnology* 37.6 (2019), pp. 645–660. ISSN: 0167-7799, 1879-3096. DOI: [10.1016/j.tibtech.2018.11.007](https://doi.org/10.1016/j.tibtech.2018.11.007). URL: [https://www.cell.com/trends/biotechnology/abstract/S0167-7799\(18\)30317-2](https://www.cell.com/trends/biotechnology/abstract/S0167-7799(18)30317-2).
- [24] Julian Schmitz, Sarah Täuber, Westerwalbesloh Christoph, Eric von Lieres, Noll Thomas, and Alexander Grünberger. “Development and application of a cultivation platform for mammalian suspension cell lines with single-cell resolution (MaSC)”. In: *bioRxiv:2020.07.14.202036* (2020). DOI: [10.1101/2020.07.14.202036](https://doi.org/10.1101/2020.07.14.202036).
- [25] Edgar Schönfeld, Sayna Ebrahimi, Samarth Sinha, Trevor Darrell, and Zeynep Akata. *Generalized Zero- and Few-Shot Learning via Aligned Variational Autoencoders*. Apr. 5, 2019. arXiv: [1812.01784](https://arxiv.org/abs/1812.01784).
- [26] Axel Theorell, Johannes Seiffarth, Alexander Grünberger, and Katharina Nöh. “When a single lineage is not enough: Uncertainty-Aware Tracking for spatio-temporal live-cell image analysis”. In: *Bioinformatics (Oxford, England)* 35.7 (2019), pp. 1221–1228. ISSN: 1367-4811. DOI: [10.1093/bioinformatics/bty776](https://doi.org/10.1093/bioinformatics/bty776).
- [27] Karen Ullrich, Edward Meeds, and Max Welling. *Soft Weight-Sharing for Neural Network Compression*. 2017. arXiv: [1702.04008](https://arxiv.org/abs/1702.04008).
- [28] Vladimír Ulman et al. “An objective comparison of cell-tracking algorithms”. In: *Nature Methods* 14.12 (2017), pp. 1141–1152. DOI: [10.1038/nmeth.4473](https://doi.org/10.1038/nmeth.4473).
- [29] Christopher K. I. Williams and Carl Edward Rasmussen. “Gaussian Processes for Regression”. In: *Advances in Neural Information Processing Systems* 8. Ed. by D. S. Touretzky, M. C. Mozer, and M. E. Hasselmo. MIT Press, 1996, pp. 514–520. URL: <http://papers.nips.cc/paper/1048-gaussian-processes-for-regression.pdf>.
- [30] Weidi Xie, J. Alison Noble, and Andrew Zisserman. “Microscopy cell counting and detection with fully convolutional regression networks”. In: *Computer Methods in Biomechanics and Biomedical Engineering: Imaging & Visualization* 6.3 (May 4, 2018), pp. 283–292. ISSN: 2168-1163, 2168-1171. DOI: [10.1080/21681163.2016.1149104](https://doi.org/10.1080/21681163.2016.1149104).
- [31] Yuanpu Xie, Fuyong Xing, Xiangfei Kong, Hai Su, and Lin Yang. “Beyond classification: Structured regression for robust cell detection using convolutional neural network”. In: *Medical Image Computing and Computer-Assisted Intervention* (International conference on medical image computing and computer-assisted intervention). Springer. 2015, pp. 358–365. URL: <https://www.ncbi.nlm.nih.gov/pmc/articles/PMC5226438/>.